

Oxidation behavior of $Ti_{0.2}Zr_{0.2}Hf_{0.2}Nb_{0.2}Ta_{0.2}C$-$M_xC$($M$=Ti, Zr, Hf, Nb, Ta) composite ceramic at high temperature

Shuai Xu(徐帅), Tao Wang(王韬), Xingang Wang(王新刚), Lu Wu(吴璐), Zhongqiang Fang(方忠强), Fangfang Ge(葛芳芳), Xuan Meng(蒙萱),Qing Liao(廖庆), Jinchun Wei(魏金春), and Bingsheng Li(李炳生)
Citation: Chin. Phys. B, 2023, 32 (**6**): 068105. DOI: 10.1088/1674-1056/ac9a38
Journal homepage: http://cpb.iphy.ac.cn; http://iopscience.iop.org/cpb

What follows is a list of articles you may be interested in

Comparative study of high temperature anti-oxidation property of sputtering deposited stoichiometric and Si-rich SiC films

Hang-Hang Wang(王行行), Wen-Qi Lu(陆文琪), Jiao Zhang(张娇), and Jun Xu(徐军)
Chin. Phys. B, 2022, 31 (**4**): 048103. DOI: 10.1088/1674-1056/ac3a61

Growth of high-crystallinity uniform GaAs nanowire arrays by molecular beam epitaxy

Yu-Bin Kang(亢玉彬), Feng-Yuan Lin(林逢源), Ke-Xue Li(李科学), Ji-Long Tang(唐吉龙), Xiao-Bing Hou(侯效兵), Deng-Kui Wang(王登魁), Xuan Fang(方铉), Dan Fang(房丹), Xin-Wei Wang(王新伟), and Zhi-Peng Wei(魏志鹏)
Chin. Phys. B, 2021, 30 (**7**): 078102. DOI: 10.1088/1674-1056/abf920

Photoelectrocatalytic oxidation of methane into methanol and formic acid over ZnO/graphene/polyaniline catalyst

Jia Liu(刘佳), Ying-Hua Zhang(张英华), Zhi-Ming Bai(白智明), Zhi-An Huang(黄志安), Yu-Kun Gao(高玉坤)
Chin. Phys. B, 2019, 28 (**4**): 048101. DOI: 10.1088/1674-1056/28/4/048101

Synthesis and characterization of β-Ga_2O_3@GaN nanowires

Shuang Wang(王爽), Yue-Wen Li(李悦文), Xiang-Qian Xiu(修向前), Li-Ying Zhang(张丽颖), Xue-Mei Hua(华雪梅), Zi-Li Xie(谢自力), Tao Tao(陶涛), Bin Liu(刘斌), Peng Chen(陈鹏), Rong Zhang(张荣), You-Dou Zheng(郑有炓)
Chin. Phys. B, 2019, 28 (**2**): 028104. DOI: 10.1088/1674-1056/28/2/028104

Excellent thermal stability and thermoelectric properties of *Pnma*-phase SnSe in middle temperature aerobic environment

Yu Tang(唐语), Decong Li(李德聪), Zhong Chen(陈钟), Shuping Deng(邓书平), Luqi Sun(孙璐琪), Wenting Liu(刘文婷), Lanxian Shen(申兰先), Shukang Deng(邓书康)
Chin. Phys. B, 2018, 27 (**11**): 118105. DOI: 10.1088/1674-1056/27/11/118105

Oxidation behavior of $Ti_{0.2}Zr_{0.2}Hf_{0.2}Nb_{0.2}Ta_{0.2}C$–$M_xC$ (M = Ti, Zr, Hf, Nb, Ta) composite ceramic at high temperature

Shuai Xu(徐帅)[1], Tao Wang(王韬)[2,†], Xingang Wang(王新刚)[3], Lu Wu(吴璐)[4], Zhongqiang Fang(方忠强)[4], Fangfang Ge(葛芳芳)[5], Xuan Meng(蒙萱)[6], Qing Liao(廖庆)[7], Jinchun Wei(魏金春)[1], and Bingsheng Li(李炳生)[7,‡]

[1] *School of Materials Science and Engineering, Southwest University of Science and Technology, Mianyang* 621010, *China*
[2] *Institute of Fluid Physics, China Academy of Engineering Physic, Mianyang* 621900, *China*
[3] *State Key Laboratory of High Performance Ceramics and Superfine Microstructure, Shanghai Institute of Ceramics, Shanghai* 200050, *China*
[4] *The First Sub-Institute, Nuclear Power Institute of China, Chengdu* 610213, *China*
[5] *Ningbo Institute of Materials Technology and Engineering, Chinese Academy of Sciences, Ningbo* 315201, *China*
[6] *Lanzhou University, Lanzhou* 730000, *China*
[7] *State Key Laboratory for Environment-Friendly Energy Materials, Southwest University of Science and Technology, Mianyang* 621010, *China*

(Received 31 May 2022; revised manuscript received 29 September 2022; accepted manuscript online 14 October 2022)

$Ti_{0.2}Zr_{0.2}Hf_{0.2}Nb_{0.2}Ta_{0.2}C$–$M_xC$ composite ceramic was prepared by hot press sintering, with the $Ti_{0.2}Zr_{0.2}Hf_{0.2}Nb_{0.2}Ta_{0.2}C$ high-entropy carbide as the main phase. Secondary phase M_xC (M = Ti, Zr, Hf, Nb, Ta) was found to be distributed relatively uniform in the composite ceramic. The oxidation behavior of the ceramic was examined after exposure to 923 K and 1173 K. Morphology of the surface and cross sections of all oxidation samples were observed. The characteristics of the oxidation behavior of the high-entropy carbide and the secondary phase M_xC were compared and analyzed. The secondary phases (such as Ti-rich carbide or Hf-rich carbide) in the material were seriously oxidized at 923 K and 1173 K, which reflects the superior oxidation performance of the high-entropy carbide. The nano high-entropy oxides with Ti, Zr, Hf, Nb, Ta, and O elements were discovered by oxidation of the composite ceramic. This research will help deepen the understanding of the oxidation mechanism of high-entropy carbide and composite ceramic.

Keywords: ceramic composites, oxidation, oxide surface, microstructure

PACS: 81.05.Mh, 81.65.Mq, 68.47.Gh, 81.40.–z **DOI:** 10.1088/1674-1056/ac9a38

1. Introduction

Key structural components of the generation IV fission reactors and future fusion reactor require new materials to fulfill their needs under extreme conditions, such as high temperatures, irradiation-induced swelling, oxidation resistance at ultrahigh temperatures, and so on.[1,2] For these reactors to serve in extreme environments, novel materials must exhibit excellent performance.

Because of the unique and intriguing physical, chemical, and mechanical properties of high-entropy carbides, they have become promising structural materials in next-generation advanced nuclear systems.[3–8] With this background, Cui *et al.* carried out irradiation experiments and creep behavior research of the high-entropy carbides, which further proved that they are useful structural materials for advanced reactor designs.[6,9]

The oxidation behavior of high-entropy carbides is another critical property for their application in advanced nuclear systems. Chu *et al.* reported the oxidation behavior of high-entropy carbides for the first time.[10] After that, research on the oxidation behavior of high-entropy carbides has gradually increased. Quaternary cation $Zr_{0.25}Hf_{0.25}Ta_{0.25}Nb_{0.25}C$ and quinary cation $Ti_{0.2}Zr_{0.2}Hf_{0.2}Nb_{0.2}Ta_{0.2}C$ were usually taken as the main research objects to study the oxidation behavior of high-entropy carbides in the temperature range of 1073 K–1873 K.[10–12] All research focused on the effect of oxidation temperature on the oxide products of high-entropy carbides. However, research results are varied, and a knowledge gap about a rigorous understanding of the oxidation processes unique to high-entropy materials still exists.

To further regulate high-temperature oxidation resistance of high-entropy carbides, some researchers have tried to dope other carbides into the high-entropy carbides to fabricate a composite ceramic. For example, 10 vol%–30 vol% of SiC was doped into quaternary cation $Zr_{0.25}Hf_{0.25}Ta_{0.25}Nb_{0.25}C$ and quinary cation $Ti_{0.2}Zr_{0.2}Hf_{0.2}Nb_{0.2}Ta_{0.2}C$ to prepare $Zr_{0.25}Hf_{0.25}Ta_{0.25}Nb_{0.25}C$–SiC and $Ti_{0.2}Zr_{0.2}Hf_{0.2}Nb_{0.2}Ta_{0.2}C$–SiC composite ceramics.[13,14] After the addition of SiC, improved oxidation resistance of the composite ceramics was obtained. It can be seen that the dope of the secondary phase can significantly affect the oxidation behavior of the high-entropy carbides. Therefore, how the inevitably induced secondary phases in the preparation process affect the oxidation performance of the high-entropy carbides is also worthy of an

†Corresponding author. E-mail: wangtaoxtc@gmail.com
‡Corresponding author. E-mail: libingshengmvp@163.com

© 2023 Chinese Physical Society and IOP Publishing Ltd

in-depth study.

In the preparation process of high-entropy carbides, equimolar mixtures of monocarbides usually have to be used as raw materials to fabricate high entropy by ball milling and then sintering.[15–17] Many parameters, such as ball milling time, temperature, pressure, and sintering time, need to be regulated in the preparation process. The materials prepared in this way will inevitably introduce some secondary phases. However, how the introduced secondary phase during the fabrication process affects the oxidation performance of high-entropy carbides has not yet been reported.

In this study, $Ti_{0.2}Zr_{0.2}Hf_{0.2}Nb_{0.2}Ta_{0.2}C$–$M_xC$ composite ceramic was prepared by ball milling following hot press sintering. The oxidation behavior and microstructural evolution below 1173 K of the composite ceramic were clarified through a comparison of the oxidation behavior between the high-entropy carbide $Ti_{0.2}Zr_{0.2}Hf_{0.2}Nb_{0.2}Ta_{0.2}C$ and the secondary phase M_xC (M = Ti, Zr, Hf, Nb, Ta). The characteristics of their oxidation products were analyzed by multiple research methods, including thermogravimetric analysis-differential scanning calorimetry (TG-DSC), x-ray diffraction (XRD), scanning electron microscope (SEM), and transmission electron microscope (TEM).

2. Experiment

2.1. Materials

Equimolar mixtures of TiC, ZrC, HfC, NbC, and TaC powders (all were supplied by Aladdin; 325 mesh and purity higher than 99.6%) were used to form a hypothetical $Ti_{0.2}Zr_{0.2}Hf_{0.2}Nb_{0.2}Ta_{0.2}C$ high-entropy carbide. Thus, 60 g of these mixtures was placed in a 500 ml ZrO_2 vial together with ZrO_2 balls. The weight of the powder-to-ball ratio is 1:10 in the present work. The mixtures were milled at a spinning rate of 200 rpm in a planetary ball mill (QM-3SP2; Nanjing NanDa Instrument Plant) to get the as-milled powders. Then, the as-milled powders were sintered by hot press at a temperature of 2000 °C for 20 min under a uniaxial pressure of 30 MPa to obtain a ceramic bulk with a diameter of about 30 mm and a height of 5 mm. The phase structure and microstructure of the high-entropy carbide were characterized using XRD (X'Pert PRO, PANalytical B.V., Netherlands) and SEM (UItra55; Carl Zeiss NTS GmbH, Germany).

Oxidation test samples were cut from the ceramic bulk as flat coupons with a dimension of 5 mm × 5 mm × 1 mm. Before the experiments, all samples were abraded with SiC paper and polished using diamond particle suspension to a 1 μm finish. To facilitate TG-DSC test and TEM analysis, some carbides were crushed into powder with a particle size of 50 μm–300 μm by mechanical method.

2.2. Oxidation test

The non-isothermal oxidation tests were performed on 10 mg powder samples from room temperature to 1473 K in dry air with a heating rate of 10 K·min^{-1} using TG-DSC (Jupiter STA 449C; NETZSCH, Germany).

The coupon was put in an open alumina crucible. Isothermal oxidation of coupons was carried out using a muffle furnace at 923 K and 1173 K in air. The oxidation times are 30 min, 70 min, and 120 min. In addition, isothermal oxidation of powder samples was carried out using a muffle furnace at 1173 K for 120 min in air.

2.3. Post test analysis

The phase structure and microstructure of the oxidized coupon surface were characterized using XRD and SEM (TM4000; Hitachi High-Technologies Corporation). After that, all oxidized coupons were embedded in epoxy resin and cut in the middle. The cross section was then polished to 1 μm finish with diamond lapping films to characterize the cross section by SEM (UItra55; Carl Zeiss NTS GmbH, Germany). To characterize the microstructure of oxidized powder sample with TEM (FEI Tecnai G2), the sample was sonicated in alcohol for 15 min, the sonicated solution was dropped on the copper mesh, and then the copper mesh was dried under an incandescent lamp at 333 K for 15 min. The nanocrystals were also analyzed using scanning TEM (STEM) coupled with energy-dispersive x-ray spectroscopy (EDX) to confirm the composition and structure of the particles.

3. Results

3.1. Characterization of as-milled powders and sintered sample

Figure 1 shows the XRD diffraction patterns of the as-milled powder and sintered sample. The diffraction peaks of the as-milled powder are very complex and are calibrated as various single-component carbides, indicating that the ball

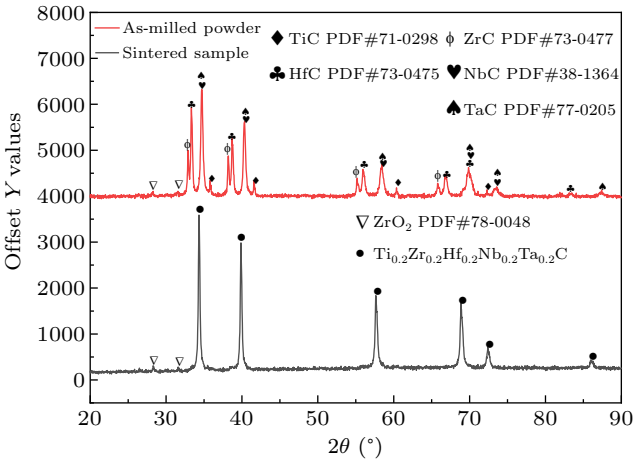


Fig. 1. XRD patterns of the as-milled powder and the sintered ceramic.

milling process only allows the mechanical mixing of raw powder without a solid solution reaction. The peak patterns of the sintered sample are very simple and consistent with the study of Cui *et al.*,[9] which indicate that the $Ti_{0.2}Zr_{0.2}Hf_{0.2}Nb_{0.2}Ta_{0.2}C$ high-entropy carbide with rock salt structure can be prepared by this method. There are two weak peaks at 28.3° and 31.6° of the as-milled powder and sintered samples, which are calibrated as ZrO_2, which indicates that the ZrO_2 ball and grinding vial pollute the as-milled powder during ball milling, which is an inevitable pollution of ball milled samples.

Figure 2 and 3 show SEM images of the polished surface of high-entropy carbide and the corresponding compositional EDS maps. As shown in Fig. 2, when the EDS characterization was performed, we found that there were some insoluble monocarbides in the sample, such as ellipsoidal Ti-rich carbide, Zr-rich carbide, and Hf-rich carbide, with size ranging from tens of microns to hundreds of microns. As we further amplified the microstructure of the materials, spherical-like Ta-rich carbide of about a few microns in size were found, as shown in Fig. 3. The reason for the formation of the Ti-rich carbide, Zr-rich carbide, Hf-rich carbide, and Ta-rich carbide remains to be explored. Although secondary phase was found in ceramics by EDS, the content of these is relatively less than the main high-entropy phase according to the XRD result. In addition, through SEM and EDS analysis, as shown in Fig. 3, it was found that there are many holes (darkest contrast area in the SEM image) in the samples, which illustrates the sintered carbide is not dense. The density of the sintered carbide is 8.44 g·cm^{-3}, which is 89.4% of the theoretical density. The theoretical density of $Ti_{0.2}Zr_{0.2}Hf_{0.2}Nb_{0.2}Ta_{0.2}C$ was estimated from the components HfC (12.74 g·cm^{-3}), TaC (14.32 g·cm^{-3}), ZrC (6.73 g·cm^{-3}), TiC (4.93 g·cm^{-3}), and NbC (8.47 g·cm^{-3}). It may be because no sintering additives are added in the sintering process, or the holding time in the sintering process is not enough. These defects or heterophases may have an important impact on the oxidation properties of high-entropy ceramics.

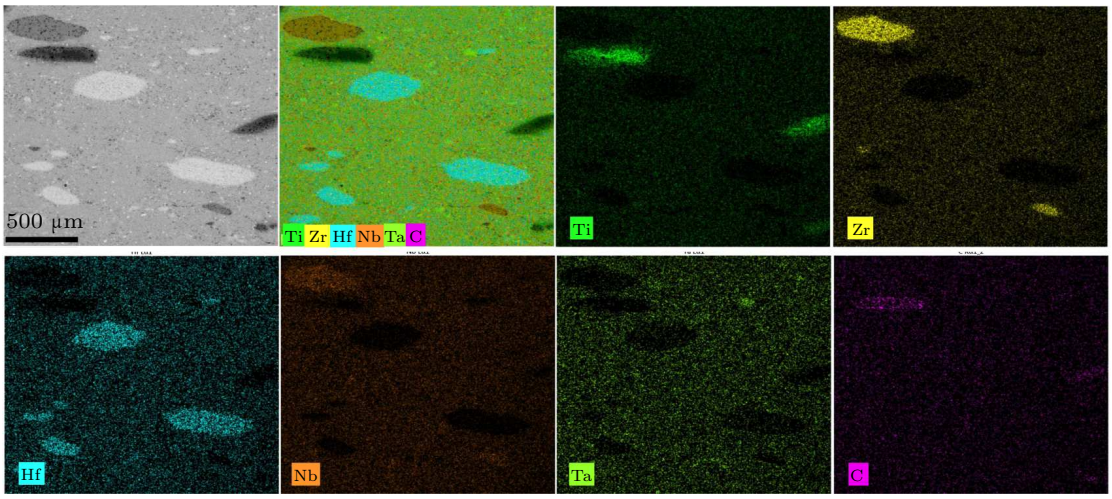


Fig. 2. SEM image (high magnification) of polished surface of $Ti_{0.2}Zr_{0.2}Hf_{0.2}Nb_{0.2}Ta_{0.2}C$–$M_xC$ composite ceramic and corresponding compositional EDS maps; Ti-rich carbide, Zr-rich carbide, and Hf-rich carbide can be seen clearly.

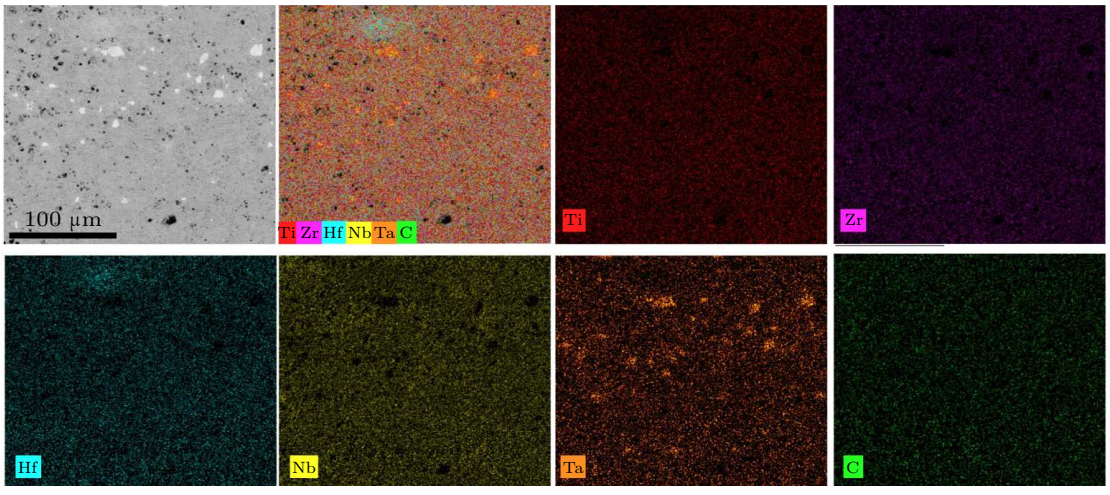


Fig. 3. SEM image (high magnification) of polished surface of $Ti_{0.2}Zr_{0.2}Hf_{0.2}Nb_{0.2}Ta_{0.2}C$–$M_xC$ composite ceramic and corresponding compositional EDS maps; Ta-rich carbide can be seen clearly.

3.2. TG-DSC analysis of the high-entropy carbide powders

The TG-DSC results of the $Ti_{0.2}Zr_{0.2}Hf_{0.2}Nb_{0.2}Ta_{0.2}C$–$M_xC$ composite ceramic powders are shown in Fig. 4. From 300 K to 834 K, there is no obvious change in mass curve of the ceramic powder, but the DSC–temperature curve shows obvious endothermic characteristics, which may be caused by the evaporation of capillary water and the oxidation of a small amount of M_xC phase. The ceramic powders have a sharp rise in weight when the temperature is higher than 834 K, which indicates that the material will undergo severe oxidation when the temperature is higher than 834 K. In addition, there is an obvious endothermic peak at 1090 K in the DSC–temperature curve, which was caused by $Ti_{0.2}Zr_{0.2}Hf_{0.2}Nb_{0.2}Ta_{0.2}C$ high-entropy carbide oxidation according to the subsequent discussion. The oxidation onset temperature for high-entropy carbide was obtained by extrapolating the tangent drawn on the steepest slope of the DSC curves to the baseline, which is an important relative measurement of the degree of oxidation stability of the materials. It can be seen from Fig. 4 that the oxidation onset temperature of $Ti_{0.2}Zr_{0.2}Hf_{0.2}Nb_{0.2}Ta_{0.2}C$ is 1040 K. Based on the TG-DSC analysis, the 923 K and 1173 K oxidation temperatures were selected to characterize the oxidation behavior of $Ti_{0.2}Zr_{0.2}Hf_{0.2}Nb_{0.2}Ta_{0.2}C$ carbide.

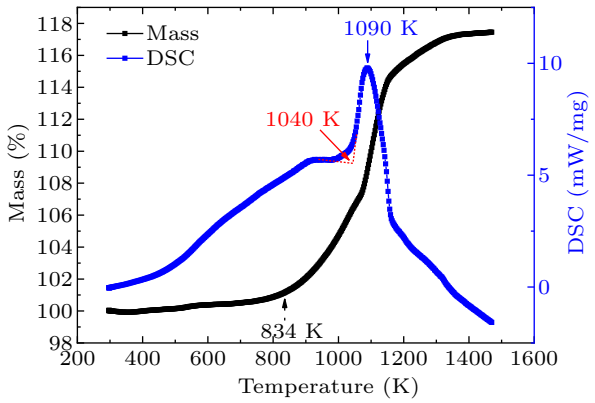


Fig. 4. TG-DSC results of the $Ti_{0.2}Zr_{0.2}Hf_{0.2}Nb_{0.2}Ta_{0.2}C$–$M_xC$ composite ceramic powders.

3.3. Evolution of microstructure after oxidation

In this section, the chemistry and microstructure of oxide(s) formed on the high-entropy carbide are characterized. XRD and SEM techniques are applied, such as EDX and SEI. The surface oxide(s) formed after 923 K oxidation are characterized in Subsection 3.3.1. Following this, the surface oxide(s) and the cross sections of the scales formed after 1123 K oxidation are characterized in Subsection 3.3.2. Due to the emergence of nano-sized oxide(s) and because the types of elements are very complex, determining the chemistry and structure of nano-sized oxide(s) is critical. Finally, in Subsection 3.3.3, the nano-sized oxide(s) of high-entropy carbide powders at 1123 K for 120 min are characterized using TEM.

3.3.1. Oxide(s) analysis at 923 K

Figure 5 shows the XRD patterns of oxidized $Ti_{0.2}Zr_{0.2}Hf_{0.2}Nb_{0.2}Ta_{0.2}C$–$M_xC$ composite ceramic at 923 K with different oxidation times. Except for the diffraction peak of the high-entropy carbide, there is no obvious oxide diffraction peak. As shown in Fig. 5, there is no oxide scale, or the oxide scale is too thin to detect. The oxide surface after oxidation at 923 K is displayed in Fig. 6. It can be seen from Figs. 6(a) and 6(c) that there are many areas with brighter or darker contrast on the surface compared to the substrate. Further analysis shows that the area of brighter or darker contrast exhibits a very loose structure, which is shown in Figs. 6(b) and 6(d). However, the substrates (Fig. 6(e)) show a relatively dense structure even after oxidation at 973 K for 120 min.

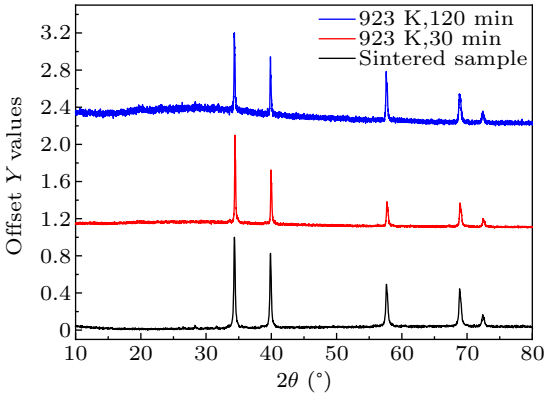


Fig. 5. XRD patterns of the sintered sample and oxidized composite ceramics at 923 K with different oxidation times.

We compared Fig. 6 with Fig. 2 and found that the darker contrast area shown in Fig. 6 was caused by the oxidation of Ti-rich carbide or Zr-rich carbide shown in Fig. 2, while the brighter contrast area shown in Fig. 6 was caused by the oxidation of Hf-rich carbide shown in Fig. 2. According to the literature, the oxidation onset temperatures of TiC, ZrC, NbC, HfC, and TaC are 973 K, 933 K, 813 K, 1005 K, and 1015 K, respectively.[18] However, the Ti-rich carbide or Zr-rich carbide and the Hf-rich carbide were oxidized at 923 K, maybe because the impurity elements in these carbides reduced their oxidation onset temperatures. It is worth noting that there is no significant change in the substrate shown in Fig. 6. We also compared Figs. 6(b), 6(d), and 6(e), and we found that the oxidation resistance of the high-entropy phase is significantly better than that of the Ti-rich carbide, Zr-rich carbide, and Hf-rich carbide. Similar research results were reported by Zhang *et al.*[19] They found that the parabolic rate constant of the (Zr,Ti,Hf,Nb,Ta)C ceramic is almost two orders of magnitude lower than that of the ZrC ceramic. They also proved that the oxidation weight gain decreases with increasing number of elemental species by comparing the oxidation behavior of (Ti,Zr,Nb)C, (Ti,Zr,Nb,Ta)C, and (Zr,Ti,Hf,Nb,Ta)C under the same isothermal oxidation. In addition, the content

of high-entropy carbide matrix in the sample is much more than that of the secondary phase; the content of the secondary phase is about 7% according to Figs. 6(a) and 6(c). Hence, although the impurities were oxidized, the peak pattern of the oxidation products in the XRD patterns (Fig. 5) is not obvious. It is worth mentioning that the oxidized local loose structure (Figs. 6(b) and 6(d)) can provide channels for the rapid diffusion of oxygen to the ceramics and further accelerate the oxidation rate of the ceramics.

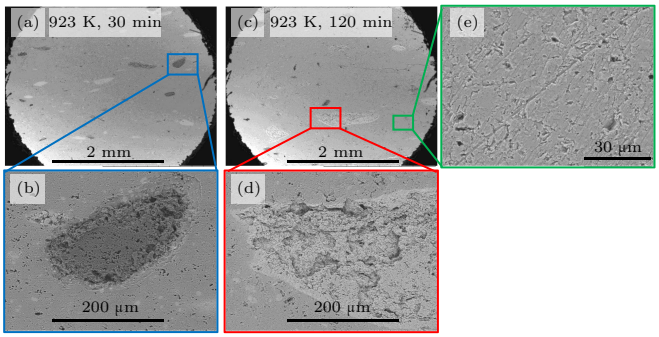


Fig. 6. (a) SEM image of oxide surface after oxidation at 923 K for 30 min and (b) the corresponding enlarged maps, and (c) for 120 min and (d) and (e) the corresponding enlarged maps.

3.3.2. Oxide analysis at 1173 K

The oxide surfaces of the $Ti_{0.2}Zr_{0.2}Hf_{0.2}Nb_{0.2}Ta_{0.2}C$–$M_xC$ composite ceramic after oxidation at 1173 K are displayed in Fig. 7. We compared Figs. 7(a) and 7(b) with Fig. 2 and found that the large-sized ellipsoidal Ti-rich carbide, Zr-rich carbide, or Hf-rich carbide heterophase in Fig. 2 can cause serious oxidation cracking and peeling of oxidation products. In addition, we compared Fig. 7(c) with Fig. 3 and found that the cauliflower-shaped oxidation products in Fig. 7(c) were caused by the oxidation of Ta-rich carbide shown in Fig. 2. It is also worth noting that nanoparticles appeared on the oxide surface after the high-entropy phase oxidation, as shown in Fig. 7(d). Therefore, it is necessary to research about the composition and structure of these nanoparticles.

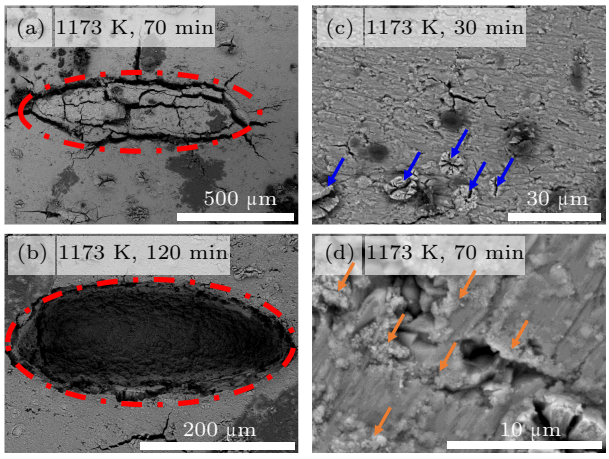


Fig. 7. SEM image of the oxide surface after oxidation at 1173 K under different oxidation times and magnifications of images: (a) 70 min, low magnification; (b) 120 min, low magnification; (c) 30 min, high magnification; and (d) 70 min, high magnification.

Figure 8 shows the XRD patterns of the oxidized $Ti_{0.2}Zr_{0.2}Hf_{0.2}Nb_{0.2}Ta_{0.2}C$–$M_xC$ composite ceramic at 1173 K at different oxidation times. The obvious oxide diffraction peak shown in Fig. 8 indicates that the oxide scale is thick. The diffraction pattern of the oxidation product is consistent with that in the literature.[10] In the literature, the oxidation products are calibrated as $(Zr_{0.5}Hf_{0.5})O_2$, $(TaNb)O_5$, and anatase TiO_2. However, the composition of the ceramic is too complex, and it may not be accurate to analyze the oxides only by using the XRD patterns. To calibrate the oxide diffraction peak, the software X'Pert HighScore Plus and MDI Jade 6 were used to identify the structure of the oxides. When we imported the tested XRD data into the software, the tetragonal Be_3P_2 (ID card: 00-029-0218) got the highest score in the X'Pert HighScore Plus, while the tetragonal $ZrO_{1.99}$ (PDF#80-2155) got the lowest FOM value in the MDI Jade 6, which indicate that the oxides may have a tetragonal structure. Setting Ti, Zr, Hf, Nb, Ta, and O as known elements, the diffraction peaks of orthorhombic $Nb_2Zr_6O_{17}$ (PDF#72-1745), orthorhombic Ta_2O_5 (PDF#71-0693), and orthorhombic $HfTiO_4$ (PDF#71-1287) are in good agreement with the tested XRD data. According to the preceding analysis, the oxidation products may have a tetragonal structure and/or an orthorhombic structure. However, it is not enough to determine the composition and structure of the oxidation products only by using the XRD method. The composition and structure of the oxidation products are worth further studying due to the diversity of elements.

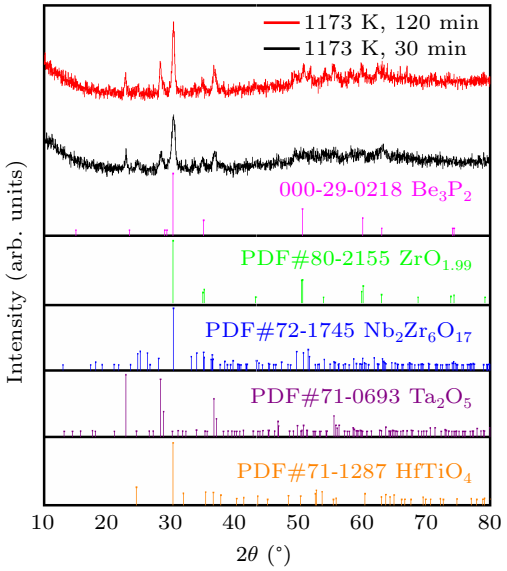


Fig. 8. XRD patterns of the oxidized ceramics at 1173 K at different oxidation times. ICCD data or PDF data of five materials are also displayed.

The SEM images of cross sections at different oxidation times at 1173 K are shown in Fig. 9. The thicknesses of the cross sections are 58 μm, 100 μm, and 135 μm at different oxidation times. It is worth noting that in the study of Chu *et al.*, the thickness of the

oxide layer of the $Ti_{0.2}Zr_{0.2}Hf_{0.2}Nb_{0.2}Ta_{0.2}C$ high-entropy phase is about 270 μm when it is oxidized at 1173 K for 120 min.[10] The thickness of the oxide layer is twice that of the $Ti_{0.2}Zr_{0.2}Hf_{0.2}Nb_{0.2}Ta_{0.2}C$–$M_xC$ composite ceramic, which may be related to the compactness of the ceramic material. The corresponding EDS elemental maps of the oxide layers formed on the sample after oxidation at 1173 K for 120 min are shown in Figs. 9(d) and 9(l). It can be seen that almost all kinds of elements in the cross sections of the oxide layer are evenly distributed, and only Ta element is distributed with dot aggregation in the whole oxide layer, which is pointed out in Fig. 9(h) as dotted circles. The relatively uniform element distribution in the oxide layer illustrates that there is no obvious delamination in the oxide layer, and the uniformly dispersed granular TaO_2 oxides in the oxide layer indicate that the oxidation mechanism of the material is internal oxidation mechanism because the distribution of TaO_2 oxides in the ceramic is consistent with that of TaC (Figs. 9(h) and 3). The internal oxidation mechanism of the high-entropy carbide is due to the material that is not dense and the loose structure provided by the oxidation of impurities, which facilitate oxygen diffusion, while the cations in the high-entropy phase diffuse very slowly due to the sluggish diffusion mechanism of high-entropy materials.[20] Similarly, Cao *et al.* propose that the inward diffusion of oxygen is the possible oxidation mechanism for the $(Hf_{0.25}Zr_{0.25}Ta_{0.25}Nb_{0.25})C$ ceramic.[14]

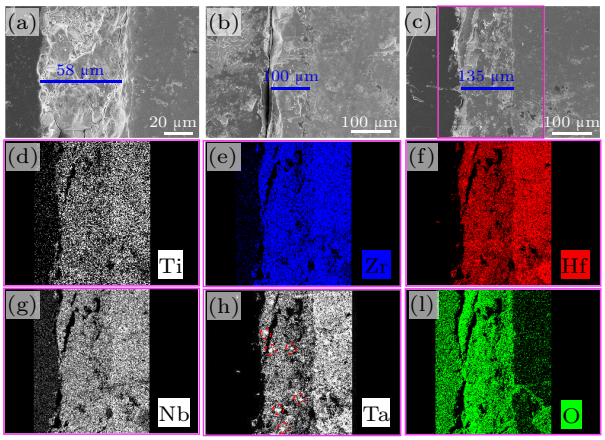


Fig. 9. SEM images of cross sections with different oxidation times: (a) 30 min, (b) 70 min, and (c) 120 min. Shown in (d)–(h) and (l) are the corresponding EDS elemental maps of the oxide layers formed on the sample after oxidation at 1173 K for 120 min.

3.3.3. Characterization of nano-sized oxide(s)

Figure 10(a) shows the TEM bright field image of oxidation products after the powder samples oxidized at 1173 K for 120 min in air. It can be seen that these oxide particles are composed of nanocrystals less than 100 nm. The corresponding EDS spectrum of the sample in Fig. 10(b) shows that the nano oxidation products contain Ti, Zr, Hf, Nb, Ta, and O elements. The compositions of nanoparticles at different positions in the TEM samples were tested, and all the EDS spectra were consistent with Fig. 10(b), which indicates that the composition of nanoparticles has been identified. Figure 11 shows the TEM images of the nano-sized oxidation product and the corresponding EDS elemental maps. An overlay of Ti, Zr, Hf, Nb, Ta, and O EDS maps is also shown in Fig. 11, which indicates that the Ti, Zr, Hf, Nb, Ta, and O elements are evenly distributed in the nano-sized oxidation product.

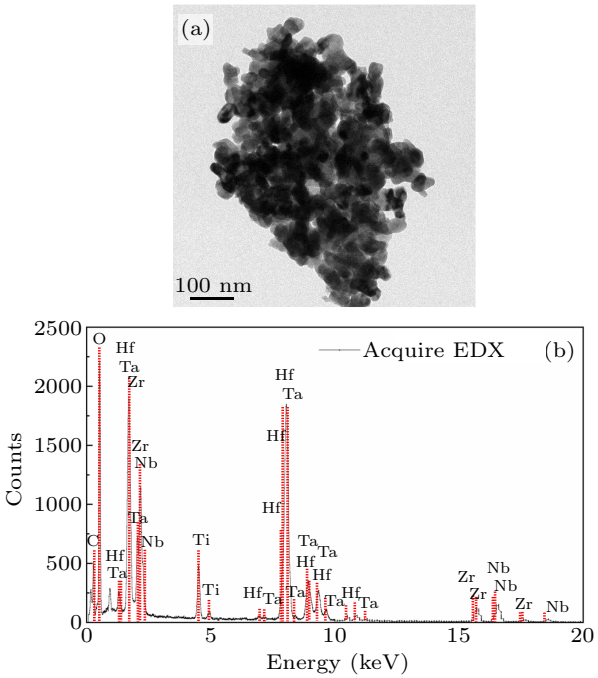


Fig. 10. (a) TEM bright field image of oxidation product after the powder samples oxidized at 1173 K for 120 min in air and (b) is the corresponding EDS spectrum of the oxidation product.

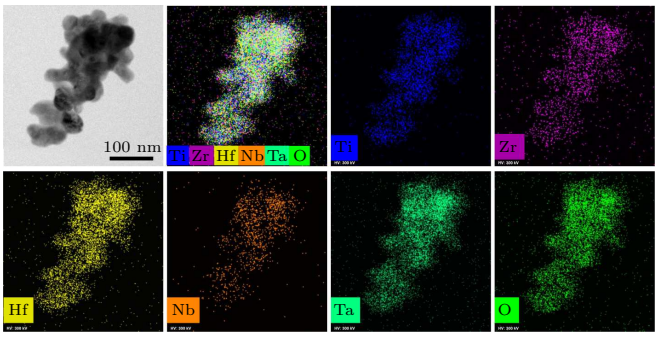


Fig. 11. TEM images showing the nano-sized oxidation product. The corresponding EDS elemental maps are also provided.

Figure 12 displays the high-angle annular dark field (HAADF) images and the corresponding fast Fourier transform (FFT) of the nano-sized oxidation product. The interplanar spacings are marked in the images, with 0.3428 nm, 0.3405 nm, 0.2571 nm, 0.2970 nm, 0.2774 nm, and 0.2651 nm, respectively. The crystal-plane index is calibrated according to the crystal structure information of the orthorhombic $Nb_2Zr_6O_{17}$ (PDF#72-1745) with cell parameters of $a = 4.092$ nm, $b = 0.493$ nm, $c = 0.527$ nm, and $\alpha = \beta = \gamma = 90^\circ$. In the calibration process, both the interplanar spacings and the crystal-plane angle are self-consistent, as

specified in Tables 1 and 2, indicating that the crystal structure information of nano-sized oxidation product is similar to that of $Nb_2Zr_6O_{17}$.

Componential analysis of the nano-sized oxidation product shows that its composition is uniform and contains all cationic elements of the high-entropy carbide. Structure analysis of the nano-sized oxidation product by XRD pattern analysis and TEM analysis (Figs. 8 and 12) demonstrates that it has an orthorhombic structure. The preceding analysis indicates that the nano-sized oxidation product is a special high-entropy oxide phase with a similar orthorhombic $Nb_2Zr_6O_{17}$ (PDF#72-1745) structure containing Ti, Zr, Hf, Nb, Ta, and O.

Table 1. Measured and calculated interplanar spacings and the crystal-plane angle in Figs. 12(a) and 12(b).

Crystal-plane index and crystal-plane angle	$(41\bar{1})$	(211)	(620)	Angle between $(41\bar{1})$ and (211)	Angle between $(41\bar{1})$ and (620)	Angle between (211) and (620)
Measured value	0.34052 nm	0.34276 nm	0.23392 nm	83.25°	41.44°	42.81°
Calculated value	0.33961 nm	0.35458 nm	0.23182 nm	83.14°	40.48°	42.67°
Relative deviation	0.26%	3.33%	0.91%	0.13%	2.37%	0.33%

Table 2. Measured and calculated interplanar spacings and the crystal-plane angle in Figs. 12(c) and 12(d).

Crystal-plane index and crystal-plane angle	(811)	$(10\bar{1}1)$	$(2\bar{2}0)$	Angle between (811) and $(10\bar{1}1)$	Angle between (811) and $(10\bar{1}1)$	Angle between $(10\bar{1}1)$ and $(2\bar{2}0)$
Measured value	0.29696 nm	0.27739 nm	0.25608 nm	68.09°	59.11°	52.80°
Calculated value	0.29441 nm	0.27030 nm	0.24473 nm	70.16°	58.40°	51.44°
Relative deviation	0.87%	2.62%	4.64%	2.95%	1.20%	2.64%

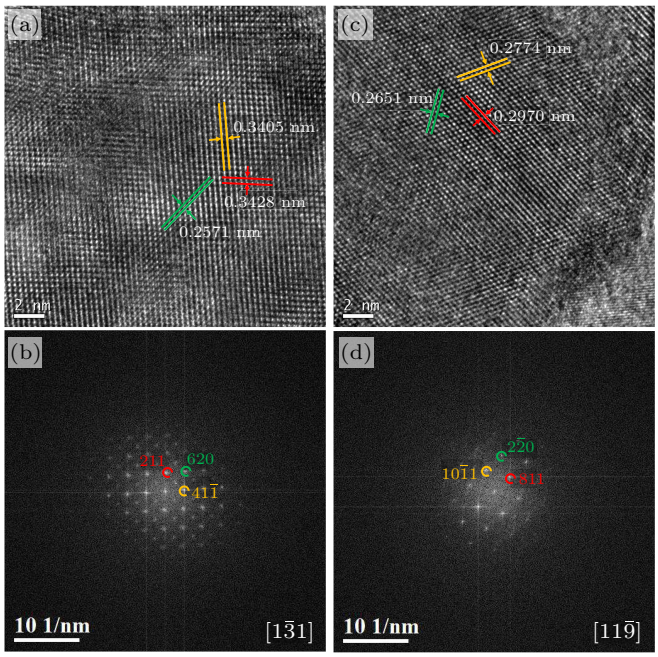


Fig. 12. (a) and (c) HAADF images of nano-sized oxidation product; interplanar spacings are shown in the images. (b) and (d) Corresponding FFT are also provided, and the crystal-plane index is calibrated according to the crystal structure information of the orthorhombic $Nb_2Zr_6O_{17}$ (PDF#72-1745).

4. Discussion

According to the results, the oxidation resistance of the secondary phases in composite ceramics is weaker than that of the high-entropy carbide. At 923 K, the large-sized secondary phases (Ti-rich carbide, Zr-rich carbide, and Hf-rich carbide) were oxidized severely with the loose surface structure, but the surface of the high-entropy phase had no obvious change, which is consistent with the XRD analysis result that no obvious peak pattern of oxidation product can be seen in Fig. 5. Backman *et al.* computationally predicted preferential oxidation of refractory ceramics, and they elucidated that group IV oxides (HfO_2, ZrO_2, and TiO_2), being most favorable, formed preferentially.[21,22] This prediction is consistent with our research that the Ti-rich carbide, Zr-rich carbide, and Hf-rich carbide, rather than the Nb-rich carbide and Ta-rich carbide, oxidized preferentially. At 1173 K, the secondary phases crack and peel off after oxidation. At the same time, the high-entropy carbide is also seriously oxidized with nano-sized oxides appearing on the oxidized surface in the high-entropy carbide area. After the composite ceramic was oxidized for 120 min, the total oxidation depth is 135 μm. There may be two reasons for such a thick oxide layer. On the one hand, the composite ceramics are not dense, providing fast channels for oxygen diffusion; on the other hand, the loose structure generated by the oxidation of the secondary phases also provides fast channels for oxygen diffusion. Therefore, enhancing compactness and reducing impurities (such as Ti-rich carbide, Zr-rich carbide, and Hf-rich carbide) in high-entropy carbide by an improved preparation method are important ways to improve its oxidation resistance.

The excellent physical and chemical properties of high-entropy carbides have attracted the attention of researchers to conduct extensive studies. Many of these researchers have studied the high-temperature oxidation of the $Ti_{0.2}Zr_{0.2}Hf_{0.2}Nb_{0.2}Ta_{0.2}C$ high-entropy carbide. There are many possible oxidation products of this high-entropy carbide, and some research results are summarized as follows:[10,11,22,23]

$$(\mathrm{Ti,Zr,Hf,Nb,Ta,})\mathrm{C}+\left(1+\frac{x}{2}\right)\mathrm{O_2}\xrightarrow{1173\ \mathrm{K}-1673\ \mathrm{K}}(\mathrm{Ti,Zr,Hf,Nb,Ta,})\mathrm{O}_x+\mathrm{CO_2},\quad(2<x<2.2),\tag{1}$$

$$10(\mathrm{Ti_{0.2}Zr_{0.2}Hf_{0.2}Nb_{0.2}Ta_{0.2}})\mathrm{C}+16\mathrm{O_2}\xrightarrow{1073\ \mathrm{K},1173\ \mathrm{K}}4(\mathrm{Zr_{0.5}Hf_{0.5}})\mathrm{O_2}+2(\mathrm{NbTa})\mathrm{O_5}+2\mathrm{TiO_2}+10\mathrm{CO(g)},\tag{2}$$

$$35(\mathrm{Ti_{0.2}Zr_{0.2}Hf_{0.2}Nb_{0.2}Ta_{0.2}})\mathrm{C}+56\mathrm{O_2}\xrightarrow{1273\ \mathrm{K}-1473\ \mathrm{K}}2(\mathrm{Zr_{0.5}Hf_{0.5}})\mathrm{TiO_4}+2(\mathrm{NbTa})(\mathrm{Zr_3Hf_3})\mathrm{O_{17}}+5\mathrm{Ti(NbTa)O_7}+35\mathrm{CO(g)},\tag{3}$$

$$(\mathrm{Ti_{0.2}Zr_{0.2}Hf_{0.2}Nb_{0.2}Ta_{0.2}})\mathrm{C}+\mathrm{O_2}\xrightarrow{1973\ \mathrm{K}}\mathrm{Zr_6Nb_2O_{17}}+\mathrm{HfTiO_4}+\mathrm{HfO_2}+\mathrm{TiTa_2O_7}+\mathrm{NbC},\tag{4}$$

$$(\mathrm{Ti_{0.2}Zr_{0.2}Hf_{0.2}Nb_{0.2}Ta_{0.2}})\mathrm{C}+\mathrm{O_2}\xrightarrow{1673\ \mathrm{K}-1873\ \mathrm{K}}(\mathrm{NbTa})\mathrm{O_5}+(\mathrm{Zr,Hf})\mathrm{TiO_4}+(\mathrm{Ti_{0.2}Zr_{0.2}Hf_{0.2}Nb_{0.2}Ta_{0.2}})\mathrm{O}_x.\tag{5}$$

Note that some of these equations do not consider the chemical ratio, mainly emphasizing the oxidation products. These equations show the complexity of the oxidation of $\mathrm{Ti_{0.2}Zr_{0.2}Hf_{0.2}Nb_{0.2}Ta_{0.2}C}$. Due to a lack of thermodynamic data to consider real systems to infer the oxidation products of the $\mathrm{Ti_{0.2}Zr_{0.2}Hf_{0.2}Nb_{0.2}Ta_{0.2}C}$ accurately, it seems inappropriate to calibrate oxidation product peak patterns in XRD of the high-entropy carbide by utilizing some known oxide phases. By combining multi-scale characterization methods, such as XRD, SEM, TEM, EDS, and HAADF, more detailed experimental results of the high-entropy carbide oxidation are shown in this research, and a reasonable scientific guess is proposed here by integrating our experimental results and the computational prediction proposed by Backman *et al.*[22,23] That is, group IV oxides ($\mathrm{HfO_2}$, $\mathrm{ZrO_2}$, and $\mathrm{TiO_2}$), being most favorable, formed preferentially. Because the elements in the high-entropy carbide are evenly distributed, the formed $\mathrm{HfO_2}$, $\mathrm{ZrO_2}$, and $\mathrm{TiO_2}$ are also evenly distributed with nano size due to the sluggish diffusion mechanism;[20] with the extension of oxidation time and the diffusion of oxygen, the oxygen partial pressure further increases to promote $\mathrm{HfO_2}$, $\mathrm{ZrO_2}$, and $\mathrm{TiO_2}$ to generate solid solutions $(\mathrm{Ti,Zr,Hf})\mathrm{O}_y$ based on the small size effect of nanoparticles,[24] and it further reacts with Ta and Nb in the materials to form $(\mathrm{Ti,Zr,Hf,Nb,Ta})\mathrm{O}_x$ high-entropy oxide. Hence, the possible mechanism of high-entropy carbide at 1173 K can be described as follows:

$$(\mathrm{Ti_{0.2}Zr_{0.2}Hf_{0.2}Nb_{0.2}Ta_{0.2}})\mathrm{C}+\mathrm{O_2}\xrightarrow{1173\ \mathrm{K}}\mathrm{HfO_2}+\mathrm{ZrO_2}+\mathrm{TiO_2}+(\mathrm{Nb,Ta})\mathrm{C}_z+\mathrm{CO_2},\tag{6}$$

$$\mathrm{HfO_2}+\mathrm{ZrO_2}+\mathrm{TiO_2}\xrightarrow{1173\ \mathrm{K}}(\mathrm{Ti,Zr,Hf})\mathrm{O}_y,\tag{7}$$

$$(\mathrm{Ti,Zr,Hf})\mathrm{O}_y+(\mathrm{Nb,Ta})\mathrm{C}_z+\mathrm{O_2}\xrightarrow{1173\ \mathrm{K}}(\mathrm{Ti,Zr,Hf,Nb,Ta,})\mathrm{O}_x+\mathrm{CO_2}.\tag{8}$$

The reaction formulas are just a conjecture and need to be further verified through more in-depth research. Simultaneous equations (6)–(8) and (1) can be obtained, which has been proposed by Zhou *et al.*[23] Overall, the $(\mathrm{Ti,Zr,Hf,Nb,Ta})\mathrm{O}_x$ high-entropy oxides can be formed by the oxidation of $\mathrm{Ti_{0.2}Zr_{0.2}Hf_{0.2}Nb_{0.2}Ta_{0.2}C}$ at 1173 K.

5. Conclusion

The $\mathrm{Ti_{0.2}Zr_{0.2}Hf_{0.2}Nb_{0.2}Ta_{0.2}C}$–$M_x\mathrm{C}$ composite ceramic was prepared by ball milling the mixture of TiC, ZrC, HfC, NbC, and TaC in equi-atomic amounts followed by hot press sintering. Then, the oxidation behavior of high-entropy carbide was investigated at 923 K and 1173 K in air. The main conclusions can be summarized as follows:

(i) The $\mathrm{Ti_{0.2}Zr_{0.2}Hf_{0.2}Nb_{0.2}Ta_{0.2}C}$ high-entropy carbide has superior oxidation performance compared with the secondary phase $M_x\mathrm{C}$ (M = Ti, Zr, Hf, Nb, Ta) in composite ceramics at high temperature.

(ii) At 923 K, only the large-sized secondary phases oxidized in composite ceramics. At 1173 K, the high-entropy carbide oxidized seriously with the formation of $(\mathrm{Ti,Zr,Hf,Nb,Ta})\mathrm{O}_x$ high-entropy oxides.

Acknowledgments

Project supported by the Doctoral Research Fund of Southwest University of Science and Technology (Grant No. 20zx7104), the Sichuan Science and Technology Program (Grant No. 2020ZYD055), and the National Natural Science Foundation of China (Grant Nos. 11905206 and 12075194).

References

[1] Zinkle S J and Was G S 2013 *Acta Mater.* **61** 735
[2] Hosemann P, Frazer D, Fratoni M, Bolind M and Ashby M F 2018 *Scr. Mater.* **143** 181
[3] Zhang R Z and Reece M J 2019 *J. Mater. Chem. A* **7** 22148
[4] Oses C, Toher C and Curtarolo S 2020 *Nat. Rev. Mater.* **5** 295
[5] Wang K, Chen L, Xu C, Zhang W, Liu Z, Wang Y, Ouyang J, Zhang X, Fu Y and Zhou Y 2020 *J. Mater. Sci. Technol.* **39** 99
[6] Han X, Girman V, Sedlak R, Dusza J, Gastle E G, Wang Y, Reece M and Zhang C 2020 *J. Eur. Ceram. Soc.* **40** 2709
[7] Dusza J, Csanádi T, Medveď D, Sedlák R, Vojtko M, Ivor M, Ünsal H, Tatarko P, Tatarková M and Šajgalík P 2021 *J. Eur. Ceram. Soc.* **41** 5417
[8] Wang Z, Li Z T, Zhao S J and Wu Z G 2021 *Tungsten* **3** 131
[9] Wang F, Yan X, Wang T, Wu Y, Shao L, Nastasi M, Lu Y and Cui B 2020 *Acta Mater.* **195** 739

[10] Ye B, Wen T, Liu D and Chu Y 2019 *Corros. Sci.* **153** 327
[11] Wang H, Han X, Liu W and Wang Y 2021 *Ceram. Int.* **47** 10848
[12] Wang Y, Zhang R Z, Zhang B, Skurikhina O, Balaz P, Araullo-Peters V and Reece M J 2020 *Corros. Sci.* **176** 109019
[13] Wang H, Cao Y, Liu W and Wang Y 2020 *Ceram. Int.* **46** 11160
[14] Wang H, Wang S, Cao Y, Liu W and Wang Y 2021 *J. Mater. Sci. Technol.* **60** 147
[15] Wei X F, Liu J X, Li F, Qin Y, Liang Y C and Zhang G J 2019 *J. Eur. Ceram. Soc.* **39** 2989
[16] Wei X F, Liu J X, Li F, Qin Y, Liang Y C and Zhang G J 2020 *J. Eur. Ceram. Soc.* **40** 935
[17] Guan S, Liang H, Wang Q, Tan L and Peng F 2021 *Inorg. Chem.* **60** 3807
[18] Wang Y and Reece M J 2021 *Scr. Mater.* **193** 86
[19] Tan Y, Chen C, Li S, Han X, Xue J, Liu T, Zhou X and Zhang H 2020 *J. Alloys Compd.* **816** 152523
[20] Moghaddam A O, Cabot A and Trofimov E A 2021 *Int. J. Refract. Met. Hard Mater.* **97** 105504
[21] Backman L, Gild J, Luo J and Opila E J 2020 *Acta Mater.* **197** 20
[22] Backman L, Gild J, Luo J and Opila E J 2020 *Acta Mater.* **197** 81
[23] Zhou J, Zhang J, Zhang F, Niu B, Lei L and Wang W 2018 *Ceram. Int.* **44** 22014
[24] Zhao J, Wang C and Wang Y 2018 *Powder Science and Engineering* (Beijing: Chemical industry press) p. 223 (in Chinese)